Basal melting and oceanic observations beneath Fimbulisen, East Antarctica

Katrin Lindbäck[1,2], Elin Darelius[3,4], Geir Moholdt[1], Irena Vaňková[5], Tore Hattermann[1], Julius Lauber[1,3], and Laura de Steur[1]

[1] Norwegian Polar Institute, Tromsø, Norway.

[2] Mid Sweden University, Östersund, Sweden.

[3] Geophysical Institute, University of Bergen, Bergen, Norway.

[4] Bjerknes Centre for Climate Research, Bergen, Norway.

[5] Los Alamos National Laboratory, Los Alamos, NM, USA.

Corresponding author: Katrin Lindbäck (katrin.lindback@miun.se)

Key Points:

- Basal melt is 1 m yr^{-1} with a short-term variability closely related with ocean velocity, indicating a shear-driven turbulent heat transfer
- The observed close relationship between melt rates and ocean velocities allows us to derive basal melt rate time series between 2010–2021
- Seasonal satellite-derived melt disagrees with in-situ melt demonstrating the importance of in-situ observations for validation

Abstract

Basal melting of ice shelves is fundamental to Antarctic Ice Sheet mass loss, yet direct observations are sparse. We present the first melt record (2017 to 2021) from a phase-sensitive radar at Fimbulisen, East Antarctica, one of the fastest flowing ice shelves in Dronning Maud Land. The observed long-term mean ablation below the central part of the ice shelf was 1.0 ±0.4 m yr^{-1}, marked by substantial sub-weekly variability ranging from 0.3 to 3.8 m yr^{-1}. 36-h filtered fluctuations in basal melt exhibit a close alignment with ocean velocity, revealing shear-driven turbulent heat transfer as the predominant driver of melt variability at sub-weekly to monthly timescales. Seasonally, basal melt rates are highest in the austral summer, when ocean temperature is higher. Our observed in-situ melt rates show threefold lower amplitudes and a 3-month delay in seasonality compared to satellite-derived melt rates, however, the long-term multi-year mean is of similar magnitude (1.0 m yr^{-1} vs 0.8 m yr^{-1}). Our detailed ice–ocean observations provide essential validation data for remote sensing and numerical models aiming to measure and project ice-shelf response to ocean forcing. In-situ measurements and continued monitoring are crucial for accurately assessing and modelling future basal melt rates, as well as understanding the complex dynamics driving ice-shelf stability and sea-level change.

1 Introduction

Changes in ice-shelf basal melting – melting of the underside of ice shelves by the ocean – is one of the largest uncertainties in future sea-level projections from the Antarctic ice sheet (IPCC, 2022). The floating ice shelves surrounding the Antarctic ice sheet restrain the seaward flow of the grounded ice upstream (Dupont & Alley, 2005). Excessive basal melting and iceberg calving can reduce the buttressing of the inland ice and lead to an acceleration of tributary ice streams (Reese et al., 2018; Shepherd et al., 2018). Increased meltwater flux from ice shelves can also have large effects on global ocean circulation, enhance ecosystem productivity, and increase sediment input into the ocean (Ingels et al., 2021). Basal melting varies substantially around Antarctica due to the different properties of the water masses entering the ice-shelf cavities (Pritchard et al., 2012; Stewart et al., 2019). The heat flux at the ice–ocean interface is determined by the thermal driving – the temperature difference between the ambient ocean temperature and the pressure dependent melting point – and the amount of turbulence in the ice-

ocean boundary layer. High ocean temperatures can cause excessive basal melting, leading to the acceleration of ice streams (Jenkins et al., 2010a; Pritchard et al., 2012). However, observations from Twaites Eastern Ice Shelf in Amundsen Sea show that high thermal driving paired with a quiescent ocean environment coincide with relatively low rates of melting (Davis et al., 2023). Hence, ocean currents are an important prerequisite for basal melting.

The basal melt rate is set by the properties and dynamics of the sub-ice shelf–ocean boundary layer – a turbulent layer that regulates the transport of heat and salt to the ice. The turbulence can be divided into two regimes: either convection or shear driven (e.g., Jenkins et al., 2010b; McConnochie & Kerr, 2018; Rosevear et al., 2021; Vreugdenhil & Taylor, 2019). For a shear-driven ice-ocean boundary layer, basal melting can be estimated by a three-equation parameterization consisting of the linearized freezing temperature expression and the balance between heat and salt fluxes at the ice-ocean interface (Holland & Jenkins, 1999; Jenkins et al., 2010b). The parameterization was confirmed to work well at cold ice-shelf cavities with strong tides (Davis & Nicholls, 2019; Nicholls, 2018), but, as expected, the parameterization is not appropriate for quiescent environments with strong stratification near the ice-shelf base (Davis et al., 2023). The close coupling between the exchanges in the ice shelf–ocean boundary layer and the large-scale circulation, driven by the resulting density gradients, is one of the key challenges for ice shelf–ocean models (Jenkins, 2021). The models that depend on observationally constrained basal drag coefficients and in-situ measurements can be used to calibrate the parameterization for a given location (Nicholls, 2018). When oceanic observations are available back in time, extrapolation is possible to acquire historic basal melt rates, as long as the parameterization has been calibrated and validated (Vaňková & Nicholls, 2022). In addition, in-situ observations are also required for the evaluation and calibration of time averaged and large-scale satellite-derived melt rates (Adusumilli et al., 2020; Moholdt et al., 2014; Rignot et al., 2013).

We present observations of basal melt from an autonomous phase-sensitive radar (ApRES; Nicholls et al., 2015) and sub-ice shelf oceanographic mooring data from a fast-flowing part (750 m yr^{-1}) of Fimbulisen ice shelf in Dronning Maud Land, East Antarctica (70° S, 0° E; Fig. 1a). The drainage basin of Fimbulisen, including the grounded ice of Jutulstraumen (191 000 km^2,

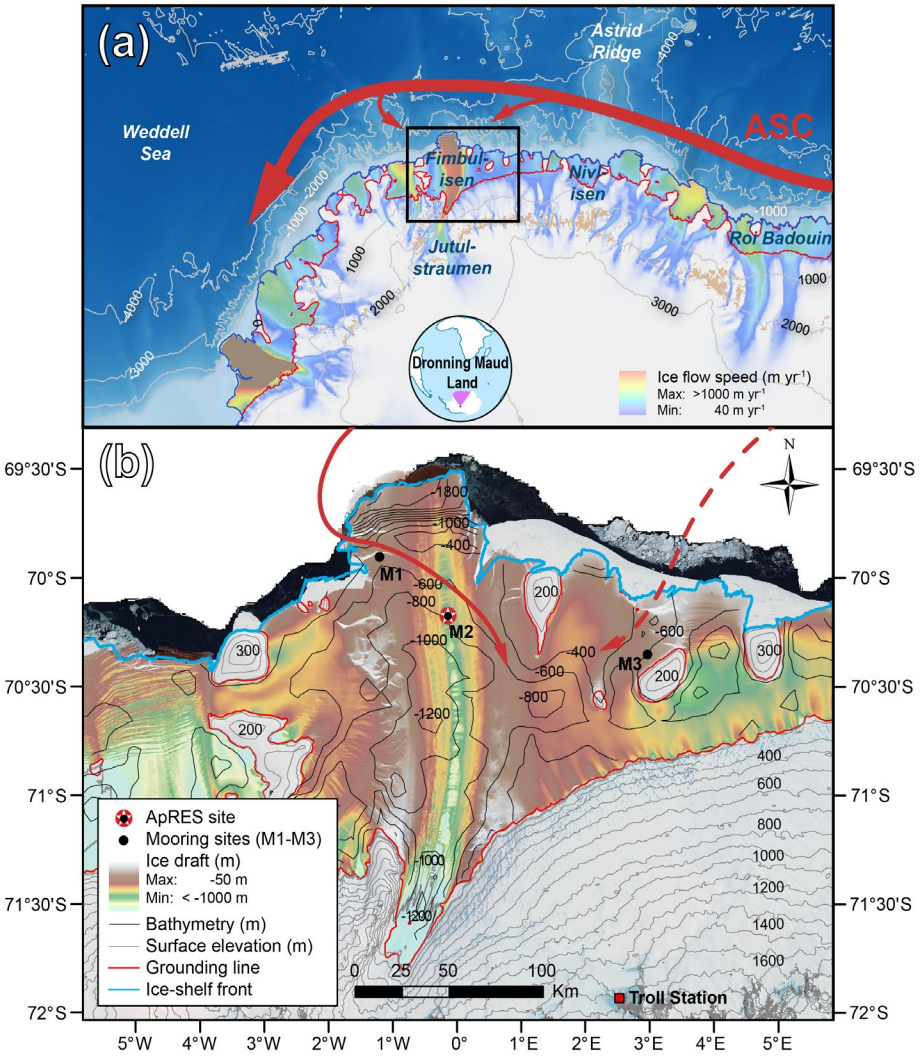

Figure 1. Study area. (a) Dronning Maud Land coast, with ice fronts (blue line), grounding zone (red line), elevation contours with bathymetric features (grey lines; Arndt et al., 2013), satellite-derived ice speed (Rignot et al., 2011) and main flow paths of the warm-deep water in the Antarctic Slope Current (ASC; Nicholls et al., 2006), marked with red arrows. (b) Map over the study site, showing the ApRES and mooring locations (labelled dots) and the position of Troll research station (red square). Ice draft (color) and surface elevation (grey, labelled contours) are derived from the REMA dataset (m a.s.l.; Howat et al., 2019), the bathymetry (labelled, black contours) is obtained from Eisermann et al. (2020), and the grounding zone and ice front are from Mouginot et al. (2017). The background image is Landsat image mosaic with some sea ice in front of the ice shelf (Bindschadler et al., 2008). Grid coordinate system is WGS-84. The detailed ice topography around mooring site M2 is shown in the Supporting information (Fig. S1).

Fig. 1a), has an estimated potential to raise global sea levels by ~70 cm (Rignot et al., 2019). The oceanographic environment in this region is part of the fresh continental-shelf regime (Thompson et al., 2018), where warmer sub-surface waters are separated from the ice front by a pronounced Antarctic Slope Front (ASF, Fig 1a). In this regime, water masses inside the ice-shelf cavity are close to the surface freezing point (–1.9 °C), while heat for basal melting is provided by an inflow of seasonally solar heated Antarctic surface water and pulses of warm deep water (with maximum temperatures of about +0.5 °C) that can propagate into the deeper part of the cavity (Hattermann et al., 2012). At greater depths, for example at the grounding line, the depression of the freezing point with increasing pressure may also be important, causing melting, and leading to the formation of potentially supercooled ice shelf water. Climate models suggest an increased access of both modified warm deep water and summer-warmed surface waters beneath ice shelves in Dronning Maud Land in future global warming scenarios (Hellmer et al., 2012, 2017; Kusahara & Hasumi, 2013). Yet, the intensity and timing of the warm-inflow episodes at depth, and the dynamic response in the cavity circulation, are still poorly understood. This study uses unique observational data of basal melt coincident with oceanic velocity and temperature data from a sub-ice shelf mooring to: (1) investigate the variability and covariation of the time series, (2) parameterize melt rates for the entire ten-year-long sub-ice shelf mooring record, and (3) compare these new results to previous studies of in-situ and satellite-derived basal melt rates beneath Fimbulisen (Adusumilli et al., 2020; Langley et al., 2014a).

2 Data and Methods

2.1 Basal melt from an autonomous phase-sensitive radar (ApRES)

In the austral summer of 2016/17, an ApRES instrument was placed on the ice-shelf surface close to the M2 mooring site (70.26 °S, 0.12 °W; Fig. 1b) and above the flank of an across-ice flow basal channel, 1.5 km wide and 75 m deep, where the ice thickness is ~400 m (Supporting information Fig. S1; Langley et al., 2014b). The instruments were re-visited, and data collected at two occasions, in the austral summer 2018/19 and then again in 2021/22. The four-year-long hourly ApRES data from 27 January 2017 to 17 May 2021 were analyzed for persistent reflectors within the ice to separate between ice thickness changes caused by vertical strain rate

and basal melting (Brennan et al., 2014; Nicholls et al., 2015). The ApRES consists of a frequency-modulated continuous wave (FMCW) radar that transmits a signal sweeping from 200 to 400 MHz over a period of 1 s to form a chirp. Basal displacement was calculated by cross-correlating the portion of the returns around the basal maxima (Supporting information Fig. S2). For a FMCW radar, the frequency of each component of the data that are acquired represents the range to a reflector via the equation $R = T\ f\ v_i/(2B)$, where v_i is the electromagnetic wave speed in ice, f is the frequency associated with the reflection at range R, T is the length of the chirp in seconds, and B is the bandwidth of the chirp. To calculate the mean vertical strain rate, we first constructed vertical-displacement time series of internal reflectors following Vaňková et al. (2020) and then calculated mean vertical velocity for each timeseries from the slope of the best line fit. The long-term displacements were then plotted as a function of depth, and a curve was fitted to these displacements to get the relative vertical displacement of the time interval (Supporting information Fig. S2d). Firn depth was extracted as a deviation from the curve fit in the upper part of the column. The vertical strain rate was estimated using quadratic fit of relative internal layer motion; the quadratic fit resulted in a statistically significant improvement over a linear fit, using an F test (F=95, Jenkins et al., 2006; Vaňková et al., 2020). We hence conclude with a high level of confidence, that the ice at site M2 is bending. The quadratic fit also resulted in a better agreement with previous estimates of radar-derived basal melt rates (Langley et al., 2014a). The quadratic fit of the internal layer displacement implies that the ice, located at a channel flank (Supporting information Fig. S1), was not in hydrostatic balance. A similar quadratic fit and order of magnitudes (~0.5 m yr^{-1}) in the long-term bending in the strain rates has been observed at, for example, Totten Ice Shelf, East Antarctica (Vaňková et al., 2021a).

The basal melt rates were calculated by subtracting the strain-thinning rates and firn-compaction rates from the observed thinning rates at the ice base. The noise in the internal displacement time series was too large to derive time-variable strain rates at the time scales of interest, therefore we had to rely on the common assumption that strain-rate variations occur at much slower time scales than basal melt-rate variations, apart from diurnal and faster tidal timescales. The latter are not the focus of this manuscript and are removed with a 36-h low-pass filter. The long-term mean depth-averaged vertical strain rate was -0.45 ± 0.48 m yr^{-1}. The error in the derived strain thinning, the primary source of error on the mean melt rate, was estimated using the quality of fit of the quadratic regression to the internal reflector displacements following Vaňková et al.

(2020). In addition, the time series of basal melt rates were 30-d land 90-d ow-pass filtered in order to study the seasonal variations.

2.2 Ocean velocity and temperature from a sub-ice shelf mooring

In austral summer 2009/10, three oceanographic moorings (M1, M2, and M3) were deployed at Fimbulisen using hot-water drilling (Fig. 1b; Hattermann et al., 2012). The moorings are hanging at the base of the shelf and are moving with the ice flow. The locations were chosen to sample the pathways where different water masses were assumed to enter the ice-shelf cavity (Nicholls et al., 2008). The bathymetric sill near M1 is at 570 m depth and close to M3 the sill it is 410 m deep. M2, where the ApRES was placed, is located further inside the cavity, over approximately 800 m seafloor depth (Fig. 1b; Supporting information Fig. S1). The M2 mooring has two sensors: an upper sensor placed 30 m below the ice-shelf base and a lower sensor placed approximately 100 m above the ocean bed and 300 m below the ice-shelf base. The sensors collected ocean-current velocity and temperature data at an hourly time interval. The upper temperature sensors at M2 unfortunately stopped working in 2016, just prior to the ApRES survey period. As for the ApRES data, the oceanic records were 36-h and 30-d low-pass filtered to remove the tidal signal and to study the seasonal variations. Noteworthy, tidal currents in the Eastern Weddell Sea region are generally weak (up to 5 cm/s at M1; Hattermann et al 2012) in comparison with other regions in Antarctica (Padman et al., 2002). Correlations between normalized 36-h basal melt rates and oceanographic observations were determined using standard correlation methods where the statistical significance level was estimated using a Monte Carlo simulation (e.g., Schreiber & Schmitz, 2000). Magnitude-square coherence was also carried out to examine correlations across timescales.

2.3 Basal melt rate parameterization

Parameterized basal melt rates were calculated from 2010 to 2021 using the three-equation parameterization in relation to observed current velocity and the seasonal temperature cycle (Holland et al., 2008; Jenkins et al., 2010b). The heat flux that drives melting at the ice–ocean interface is, to the first order, set by the local thermal driving $T^* = T_w - T_f$, the difference in ocean temperature relative to local melting point, and the friction velocity u^*, related to the current speed U that supports turbulent mixing near the ice-shelf base (Holland et al., 2008). Higher melt

rates are expected to increase the current strength locally, because of the circulation response to freshwater input. Nevertheless, for a first assessment we may take ocean temperature and current strength as two independent externally-forced parameters. With the three-equation parameterization, we can consider the melt rate curve m to be a product of T^* (Jenkins et al., 2010b):

$$m\,\rho_i L_i = m\,\rho_i\,c_i\,T_{*i} - \rho_w c_w C_d\,\Gamma_{TS}\,UT^* \quad (1)$$

which can be rearranged to the following:

$$m = \left\{\frac{-\rho_w\,c_w\,C_d\,\Gamma_{TS}}{\rho_i(L_i - c_i\,T_{*i})}\right\} UT^* = C_0 * UT^* \quad (2)$$

where C_d is the drag coefficient, Γ_{TS} is the heat exchange coefficient, L is the latent heat of fusion of ice, c is the specific heat capacity, ρ is the density, and the subscripts i and w refer to ice and water respectively. T^*_i represents the difference in ice temperature relative to the local melting point. We assume the thermal exchange coefficients to be constant, which implies that the term in braces, which we denote C_0 is approximately constant, as it depends only weakly on the ice temperature relative to the seawater freezing point. We estimate C_0 using the mean values of basal melt (2017–2021) and M2 upper current velocity (2017–2021) and temperature (2009–2016). No significant trend in temperature over the period was observed and the temperature variability for the pre-ApRES period only influences the melt parameterization peaks slightly (Supporting information Text S1, Fig. S4). Then, we use Eq. (2) to parameterize past melt rates using the 30-d filtered current speeds 2010 to 2021 and the long-term seasonal temperature cycle at the M2 upper sensor 2010 to 2016. We also parameterized melt using observed temperature at the upper sensor for the pre-ApRES period. To fill in the gaps where no data is available for the upper sensor, we used the current speeds of the lower sensor. We also calculated 90-d parameterized melt (2009–2021) to compare with ApRES and satellite-derived basal melt rates from an Antarctic-wide study at 10 km resolution (Adusumilli et al., 2020). For local comparison, we used the grid point closest to M2.

Inserting values for the material constants in Eq. (1), we calculated the tunable effective thermal Stanton number $C_d\Gamma_{TS}$:

$$C_d\Gamma_{TS} = -C_0\,\rho_i(L_i - c_i T_{*i})/\rho_w c_w \quad (3)$$

The Stanton number represents the ratio of the heat transfer due to turbulent momentum transfer to the heat transfer due to molecular diffusion across the boundary layer between the ocean and the ice sheet.

3 Results

3.1 Variability of basal melting and oceanic observations

The 36-h low-pass filtered ApRES-derived melt rate varied from 0.3 to 3.8 m yr^{-1}, where the largest melt rate occurred in early spring 2017 (24 Sept. 2017; Fig. 2a). The 30-d low-pass filtered basal melt rates show a variable level of seasonal variation (Fig. 3a), where the largest melt rates occurred in austral spring to autumn (October to March) and lowest in winter (May to July). The long-term mean basal melt rate was 1.0 m yr^{-1} ±0.4 m yr^{-1}, marginally higher than earlier estimates from in-situ and satellite-based techniques from the same area (ranging from 0.8 to 0.9 m yr^{-1}; Tabl. 1). Substantial interannual variability is seen during the four years: the annual averaged melt rate was largest in 2017 at 1.3 m yr^{-1}, decreasing in the following years to 1.1 m yr^{-1} in 2018 and 0.9 m yr^{-1} in 2019 and 2020. No thickening due to intermittent accretion of marine ice (Vaňková et al., 2021b) was observed at any time.

The 36-h low-pass filtered current speeds varied between 0 and 17 cm s^{-1} at the upper sensor (30 m below the ice-shelf base) with an average of 4 cm s^{-1} (Fig. 2b), and between 0 and 34 cm s^{-1} at the lower sensor (close to the seabed) with the same average as the upper sensor (Fig. 2c). The prevailing ocean flow direction is towards northeast. A reversal of the current direction at both sensors occurred during the period with highest current speeds (October 2017; Fig. 2ce). The 30-d low-pass filtered current speeds show substantial interannual variability and a mean seasonality with higher current speeds during austral summer for the lower sensor (Fig. 3c and Fig. 4b) and in 2010 and 2017 for the upper sensor (Fig. 3b and Fig. 4b). The 36-h low-pass filtered temperatures varied between –1.9 and –1.4 °C at the lower sensor with an average of –1.8 °C (Fig. 2d). 30-d lowpass filtered temperatures at the upper sensor in 2010 to 2016 varied from –2.1 to –1.9 °C, with an average of –2.0 °C (Fig. 4b). 30-d lowpass filtered temperatures at the lower sensor in 2010 to 2021 varied from –1.9 to –1.7 °C, with an average of –1.8 °C (Fig. 3d

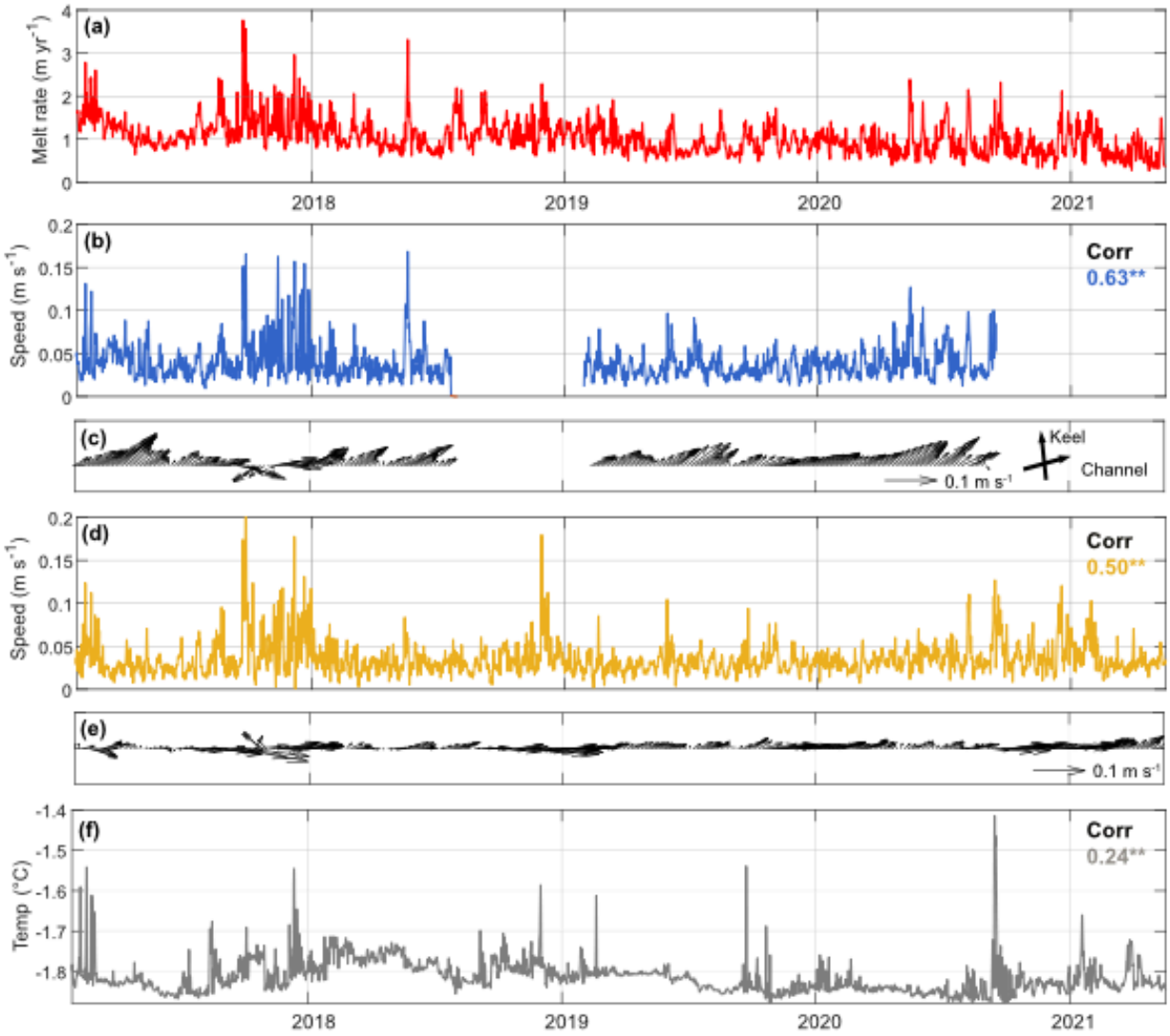

Figure 2. Basal melting and oceanic observations at the M2 mooring site from 27 January 2017 to 17 May 2021. 36-h low pass filtered timeseries of (a) ApRES melt rates and ocean current strengths at the M2 (b) upper and (d) lower sensor with current vectors from the M2 (c) upper and (e) lower sensor. The thick black arrows in (c) indicate the principal axis of the ice-shelf keel and basal channel (north is upward; Fig. 1b; Supporting information Fig. S2). (f) Ocean temperature at the M2 lower sensor. Correlation between basal melt and upper sensor currents (blue), lower sensor currents (yellow), and lower sensor temperatures (grey) are displayed in the panels (** $p < 0.01$).

and Fig. 4b). Higher temperatures occurred in austral summer season compared to the winter months (May to July) for both temperature sensors (Fig. 3cd).

3.2 Correlation between basal melting and oceanic observations

We found strong and significant correlation between normalized 36-h filtered records of basal melt rates and current strengths for the upper sensor ($r = 0.63$, $p < 0.01$), and moderate correlation for the lower sensor ($r = 0.50$, $p < 0.01$). These correlations also hold for longer monthly timescales (Supporting information Fig. S3) and show that basal melt rates and ocean velocities are closely linked, where enhanced turbulence may increase the melt rates (Eq. (2)). The correlation between the upper and lower mooring currents was also significant and moderate ($r = 0.51$, $p < 0.01$) with a vertically coherent flow variability and unidirectional current vectors (Fig. 2ce), suggesting that the observed melt rate variability is primarily a response to regionally forced velocity fluctuations, rather than being a driver of those, as melt-enhanced buoyant plumes that rise along the sloping ice base would primarily increase the flow speed at the upper sensor.

The historic mooring records (2010–2016), show a similar moderate, significant correlation between the upper and lower current sensors at monthly timescale ($r = 0.44$, $p < 0.01$) demonstrating that much of the flow variability is depth independent throughout the observational record. The four-year mean seasonal signal in melt rates (2017–2021) is in phase with the multi-year mean temperature signal (2010–2016; Fig. 3ad). Although they are derived from different time periods, it is likely that a seasonal signal in temperature was also present post-2016, and therefore contributed to the observed seasonal cycle in the melt rate. The correlation between the basal melt rates and 36-h filtered temperatures at the lower sensor is low ($r = 0.24$, $p < 0.01$; Supporting information Fig. S3). In addition, the temperature data up to 2016 (Fig. 4c) show no correlation between the upper and lower sensors. Inflow of warm deep water is expected to follow the bathymetry further into the cavity, rather than providing direct heat for melting at M2 (Hattermann et al., 2014). However, such inflow events may be associated with an increase in the circulation strength and hence higher melting driven by larger flow speeds. An example of such an inflow event associated with high melting and current direction reversal occurred in October 2017 (Fig, 2bc). This is discussed further below.

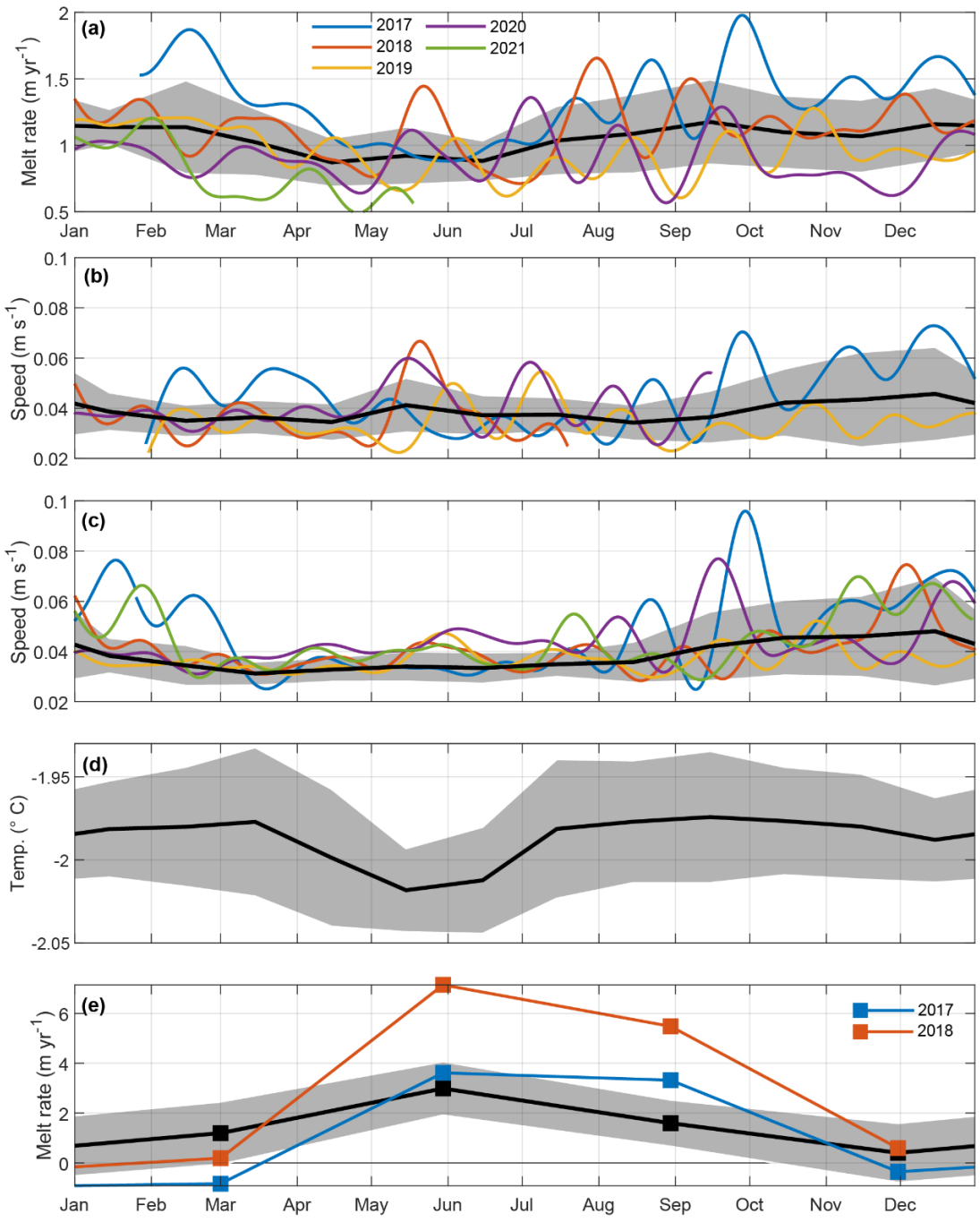

Figure 3. Monthly mean (black line) and standard deviation (grey shading). (a) Basal melt rates (2017–2021), ocean current strengths at M2 (b) upper (2010–2020) and (c) lower sensor (2010–2021), (d) ocean temperatures at the M2 upper sensor (2010–2016). (e) Satellite-derived basal melt rates, 90-d average (2010–2018) from Adusumilli et al. (2020).

3.3 Basal melt rate parameterization

When calibrating the three-equation parameterization using the available observations (Fig. 4), we find the best fit to the observed ApRES data is achieved when using the current speeds and the mean monthly temperature cycle (2010–2016) from the upper sensor (blue line; Fig. 4a). For comparison, parameterized melt using observed temperature at the upper sensor for the pre-ApRES period is also shown (purple line; Fig. 4a). The data gap in the upper current velocities in 2016 was filled using the lower-sensor current data (yellow line; Fig. 4a). However, for the overlapping ApRES period, the melt rates estimated using the parameterization and velocities from the lower sensor have amplitude peaks approximately twice as high as the observations, whereas the long-term melt is not affected giving a closer match around 1 m yr^{-1} (Fig. 4d). We justify the use of the current speeds from the lower sensor to fill in the data gaps for the upper sensor by the significant correlation between the two current sensors, the agreement between the two alternative parameterizations (blue and yellow lines) for the pre-2016 period, and the identical long-term mean velocities (0.4 m yr^{-1}). The uncertainty in the parameterized melt was calculated using standard analytical error propagation (Supporting information Text S1), resulting in an error of ±0.6 m yr^{-1}.

The 30-d parameterized basal melt rates show no significant long-term linear trends, but rather an interannual variability, where the periods with higher melt correspond to periods with higher current speeds in the ice-shelf cavity (Lauber et al., 2023a). In the austral summer of 2010 to 2011, the parameterized melt rates are up to 3.1 m yr^{-1}, compared to 2.0 m yr^{-1} in 2017, when the ApRES-derived melting was largest. In this period, high current speeds at both the upper sensor and the lower sensor were observed (Fig. 4b). The following years 2012 to 2015 represents a period with lower parametrized basal melt (~1 m yr^{-1}) and no apparent seasonal cycle, corresponding to a period of reduced deep warm water inflow into the cavity (Fig. 4c; Lauber et al., 2023a). At the end of 2016, the parameterized melt rates increased again and show a stronger seasonality, consistent with a shift toward more persistent deep warm inflow registered at the sub-ice shelf mooring M1 close to the Fimbulisen ice-shelf front (Fig. 1b; Lauber et al., 2023a). We calculated the tunable effective thermal Stanton number, which sets the rate of heat transfer, to be 10^{-4}, which is in the same order of magnitude as in previous studies

that modelled basal melt rates for cold ice-shelf cavities (e.g., Jenkins et al., 2010b; Jenkins, 2011).

4 Discussion

Our results show a prominent covariation between observed basal melt rates and ocean velocity at sub-weekly to monthly timescales. A pronounced correspondence with (long-term mean) sub-ice shelf ocean temperatures on the seasonal timescale is also observed. The significant correlation between melt rates and current speeds and the overall good agreement of the parameterization with the observed melt rate suggest that shear-driven heat transfer is dominant at this site. For a conductively driven turbulent regime, there would be stronger stratification within the ice-ocean boundary layer, influencing the heat transfer. Considering an observed ice temperature gradient of 0.5 °C m^{-1} at M2 (unpublished data), the basal melting from conductive heat fluxes would only be ~0.1 m yr^{-1}, which is well below observed melt rates.

In numerical models, sub-ice shelf ocean velocity at Fimbulisen is generally controlled by the ice-shelf cavity overturning circulation, which is driven by buoyancy fluxes due to melting, particularly at the grounding line, and horizontal pressure gradients along the ice front (Hattermann et al., 2014). Additional processes may contribute to or modify melting and we discuss some of these below: At Nivlisen, an ice shelf 300 km east of Fimbulisen (Fig. 1a), high basal melting was observed 4 km from the ice-shelf front, linked to the intrusion of solar heated surface waters during summer (Lindbäck et al., 2019). At Fimbulisen, solar heated water masses have been observed below the ice front (Hattermann et al., 2012) but we expect these water masses to have lost most of their heat when reaching M2. The lower density of this water mass may nevertheless aid to separate the ice base from colder ice-shelf water that ascends from deep inside the cavity, preventing marine ice accretion. At the Roi Baudouin Ice Shelf, 800 km east from Fimbulisen (Fig. 1a), basal melting was suggested to be enhanced at the deep grounding line, 75 km from the calving front, by the generation of topographic waves originating from the ice shelf front linked to tidal flows (Sun et al., 2019). Tides are not very strong at Fimbulisen, with tidal flows <5 cm s^{-1} at the M2 site and we expect these not to be a major driver for basal melting at M2. At the Filchner-Ronne Ice Shelf, 1500 km west of Fimbulisen, a seasonal melt signal was observed related to the propagation of dense water from the western ice-shelf front

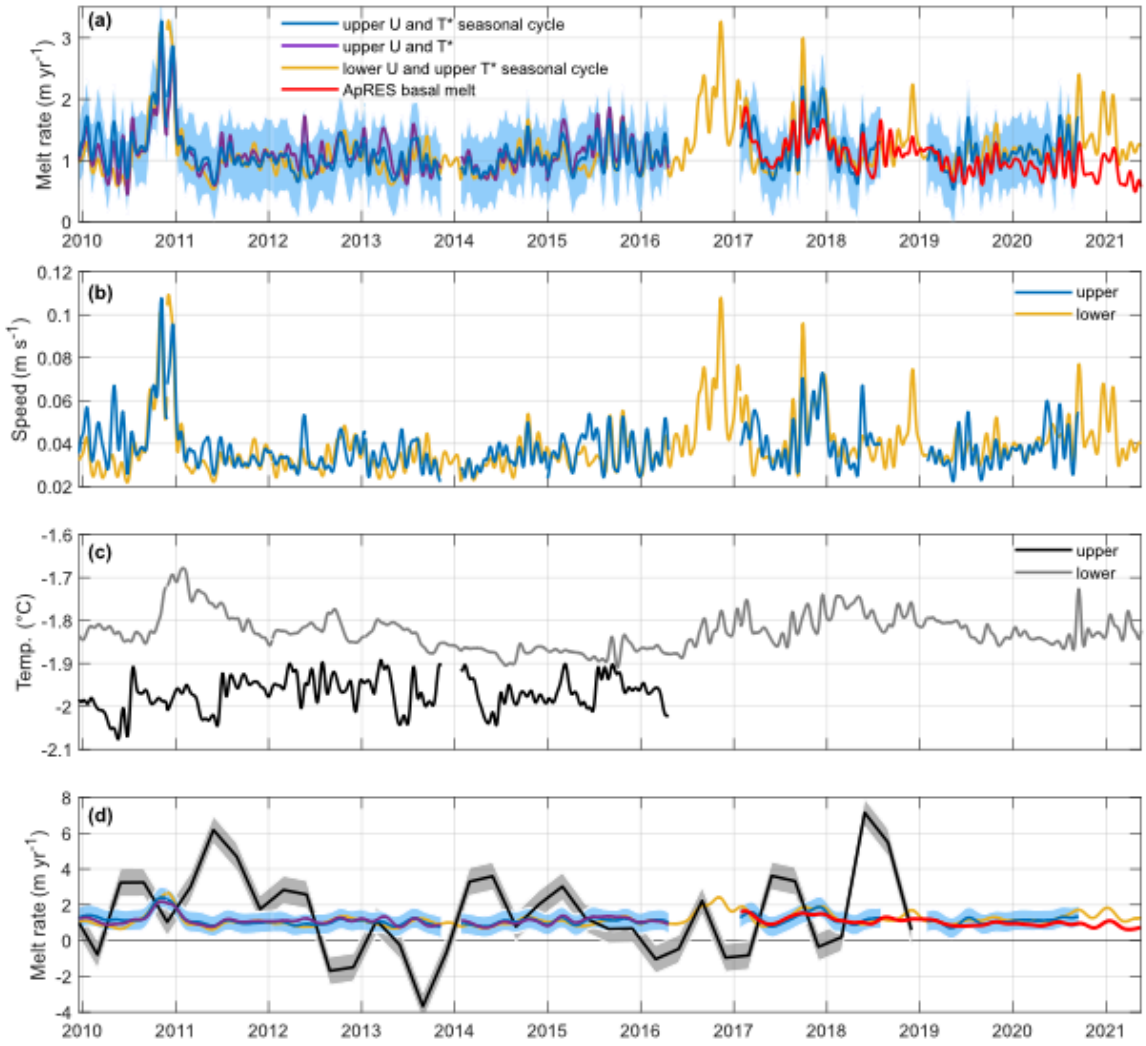

Figure 4. (a) Times series of basal melt rates from the parameterizations, and the ApRES (red line). The different parameterizations are based on the current speeds and mean monthly temperature cycle (2010–2016) from the upper sensor (blue line), current speed and temperature from the upper sensor (purple line), and the current speed from the upper sensor and temperature from the lower sensor (yellow line). The uncertainty of the parameterization with the best fit (blue line) is shown in light blue shading. (b) Ocean current strengths at M2 upper (blue) and M2 lower (yellow) sensor. (c) Ocean temperatures at M2 upper (black line) and lower (grey line) sensor. Time-series shown in (a-c) are 30-d low-pass filtered. (d) 90-d mean local satellite-derived basal melt rates (black line), with uncertainty (grey shading; Adusumilli et al., 2020). Parameterized and ApRES melt rates from panel (a) are also shown (90-d filtered).

into the cavity (Vaňková & Nicholls, 2022). However, at Fimbulisen the continental shelf break is mostly situated within the ice shelf cavity, and there is no formation of high-salinity shelf water here. Lauber et al. (2023a) observed deep warm inflow events at the M1 mooring site from 2010 to 2012 associated with reduced wind-driven downwelling in front of Fimbulisen. This warm inflow reached the lower sensor at M2 in 2011 but was not observed at the upper temperature sensor (Fig. 4c). Since 2016, a more sustained warm inflow occurred at M1 linked to increased subpolar westerlies and reduced sea ice. This was associated with enhanced current velocities (Lauber et al., 2023a) and was in general agreement with the high basal melt in 2017 as presented here (Fig. 2a, 3a), as well as increased warm water presence at depth at M2 (Fig. 4c). We hypothesize that deep warm inflows during these periods could cause a general speed-up of the cavity overturning via melting at the grounding line, which then lead to higher melting at M2 due to higher velocities.

The multi-year mean satellite-derived basal melt rates at Fimbulisen (Adusumilli et al., 2020; Rignot et al., 2013) are slightly smaller but close to our long-term mean basal melt rates (~1 m yr^{-1}; Tabl. 1). However, the satellite-derived melt rates show higher melt rates in winter compared to summer (Fig. 3e) and hence, are out of phase with the observed seasonality in the ApRES record. In addition, the amplitude of variability of the satellite-derived melt rates is about three times larger than our in-situ observations (Figs. 3, 4d). The satellite-derived melt rates also indicate substantial freezing at times (i.e., negative melt rates, Fig. 4d), which is not supported by our local observations at M2. However, it may not be excluded that freezing occurs elsewhere surrounding M2 given the larger 10 km footprint of the satellite data (Tabl. 1). The higher variability in the satellite-based record is not unexpected as satellite-based basal melting is derived as a residual of a series of other varying parameters such as surface height, surface mass balance, firn density, ice dynamics and sea level. Any error in these parameters will be reflected in the derived basal melt time series. One reason for underestimation of melting in summer and overestimation in winter can be more summer precipitation and/or less winter precipitation than regional climate models indicate. Another reason can be a potential seasonal height bias in the satellite altimetry data due to more radar signal penetrating into dry winter snow than into melt-affected summer snow, as observed for comparable climates on the Greenland ice sheet (Nilsson et al., 2015) and on an Arctic ice cap (Morris et al., 2022). Changes in ice dynamics could also have an impact (Boxall et al., 2022), but are relatively small on seasonal timescale in most of

Antarctica (Greene et al., 2020). In line with our findings, an overestimation of the seasonal variability in satellite-derived melt rates compared to in-situ measurements have been reported from Filchner-Ronne Ice Shelf (Vaňková & Nicholls, 2022) and Totten Ice Shelf (Vaňková et al., 2023). Consequently, the detectability threshold of temporal melt rate variability through satellite methods is yet uncertain. Future improvement and validation of satellite-based records of basal melting need to not only consider ice-ocean interactions, but also near-surface climate processes that influence the estimation technique. Coincident measurements of surface height and snow properties would help towards this. For ice shelves with considerable subglacial topography, like Fimbulisen, distributed ApRES measurements are also needed to address the spatial variability in basal melting, connecting the different scales of in-situ and satellite observations.

Study	Basal melt rates	Survey period	Method	Grid
Rignot et al. (2013)	0.9 ± 0.2 m yr^{-1}	2003–2008	Satellite	1 km
Langley et al. (2014)	0.84 ± 0.01 m yr^{-1}	2009–2010	In-situ radar	< 0.5 km
Adusumilli et al. (2020)	0.8 ± 0.8 m yr^{-1}	2010–2018	Satellite	10 km
This study	1.0 ± 0.4 m yr^{-1}	2017–2021	In-situ radar	< 0.5 km

Table 1. Basal melt rates measured at Fimbulisen (M2 site) with in-situ radar and estimates using satellite techniques.

5 Conclusions

The mean melt rate obtained from the four years of ApRES data on Fimbulisen was around 1 m yr^{-1}, slightly larger than previous in-situ and satellite-derived estimates and showed a substantial interannual variability during this period. The record of basal melt rate shows a close correspondence with ocean currents at sub-weekly to monthly timescales, with peaks corresponding to when ocean velocities under the ice shelf were largest. Ocean temperatures corresponded with the melt rate variability on seasonal timescales. On shorter timescales, the contribution of the observed temperature variability in the parameterized melt rates is small

compared to the effect of the current variability. We conclude that short-term basal melt rates at this location in the center of the ice shelf are primarily forced by higher ocean velocities and that the melting is dominated by shear-driven heat transfer. Compared to a satellite-based record of basal melt, seasonal peaks in basal melt rates occurred towards the austral summer rather than in winter, and the magnitude was threefold lower. The difference found between in-situ observations and remotely sensed estimates demonstrate that in-situ observations are necessary for improving remote sensing estimates and for developing our understanding of the ice shelf-ocean interaction and its response to climate change.

Acknowledgments

This work was part of the iMelt (Ocean-ice shelf Interaction and channelized Melting in Dronning Maud Land) project, funded by the Research Council of Norway (project number 295075). IV received funding from the Laboratory Directed Research and Development program of Los Alamos National Laboratory under project number 20220812PRD4. We would like to thank NPI logistic heads and personnel who helped us in the field. For the REMA data set we acknowledge the DEMs by the Byrd Polar and Climate Research Center and the Polar Geospatial Center.

Open Research

The processed data of basal melt rates are available at https://doi.org/10.21334/npolar.2023.1bbf3c47 (Lindbäck et al., 2023). Daily mooring observations at M2 are available at https://doi.org/10.21334/npolar.2023.4a6c36f5 (Lauber et al., 2023b).

References

Adusumilli, S., Fricker, H. A., Medley, B., Padman, L., & Siegfried, M. R. (2020). Interannual variations in meltwater input to the Southern Ocean from Antarctic ice shelves. *Nature Geoscience*, *13*(September 2020), 616–620. https://doi.org/10.1038/s41561-020-0616-z

444 Arndt, J. E., Schenke, H. W., Jakobsson, M., Nitsche, F. O., Buys, G., Goleby, B., et al. (2013).
445 The International Bathymetric Chart of the Southern Ocean (IBCSO) Version 1.0 — A
446 new bathymetric compilation covering circum-Antarctic waters. *Geophysical Research*
447 *Letters*, *40*, 3111–3117. https://doi.org/10.1002/grl.50413

448 Brennan, P. V, Lok, L. B., Nicholls, K., & Corr, H. (2014). Phase-sensitive FMCW radar system
449 for high-precision Antarctic ice shelf profile monitoring. *IET Radar Sonar Navigation*,
450 *8*(7), 776–786. https://doi.org/10.1049/iet-rsn.2013.0053

451 Bindschadler, R., Vornberger, P., Fleming, A., Fox, A., Mullins, J., Binnie, D., et al. (2008).
452 Remote Sensing of Environment The Landsat Image Mosaic of Antarctica. *Remote*
453 *Sensing of Environment*, *112*(12), 4214–4226. https://doi.org/10.1016/j.rse.2008.07.006

454 Boxall, K., Christie, F. D. W., Willis, I. C., Wuite, J., & Nagler, T. (2022). Seasonal land-ice-
455 flow variability in the Antarctic Peninsula. *The Cryosphere*, *16*(10), 3907–3932.
456 https://doi.org/10.5194/tc-16-3907-2022

457 Davis, P. E. D., & Nicholls, K. W. (2019). Turbulence Observations Beneath Larsen C Ice Shelf,
458 Antarctica. *Journal of Geophysical Research: Oceans*, *124*(8), 5529–5550.
459 https://doi.org/10.1029/2019JC015164

460 Davis, P. E. D., Nicholls, K. W., Holland, D. M., Schmidt, B. E., Washam, P., Riverman, K. L.,
461 et al. (2023). Suppressed basal melting in the eastern Thwaites Glacier grounding zone.
462 *Nature*, *614*(7948), 479–485. https://doi.org/10.1038/s41586-022-05586-0

463 Dupont, T. K., & Alley, R. B. (2005). Assessment of the importance of ice-shelf buttressing to
464 ice-sheet flow. *Geophysical Research Letters*, *32*, 1–4.
465 https://doi.org/10.1029/2004GL022024

466 Eisermann, H., Eagles, G., Ruppel, A., Smith, E. C., & Jokat, W. (2020). Bathymetry Beneath
467 Ice Shelves of Western Dronning Maud Land, East Antarctica, and Implications on Ice
468 Shelf Stability. *Geophysical Research Letters*, *47*(12).
469 https://doi.org/10.1029/2019GL086724

470 Greene, C. A., Gardner, A. S., & Andrews, L. C. (2020). Detecting seasonal ice dynamics in
471 satellite images. *Cryosphere*, *14*(12), 4365–4378. https://doi.org/10.5194/tc-14-4365-
472 2020

Hattermann, T, Smedsrud, L. H., Nøst, O. A., Lilly, J. M., & Galton-fenzi, B. K. (2014). Eddy-resolving simulations of the Fimbul Ice Shelf cavity circulation: Basal melting and exchange with open ocean. *Ocean Modelling*, *82*, 28–44. https://doi.org/10.1016/j.ocemod.2014.07.004

Hattermann, Tore, Nøst, O. A., Lilly, J. M., & Smedsrud, L. H. (2012). Two years of oceanic observations below the Fimbul Ice Shelf, Antarctica. *Geophysical Research Letters*, *39*(L12605). https://doi.org/10.1029/2012GL051012

Hellmer, Hartmut H, Kauker, F., Timmermann, R., & Rae, J. (2012). Twenty-first-century warming of a large Antarctic ice-shelf cavity by a redirected coastal current. *Nature*, *485*, 225–228. https://doi.org/10.1038/nature11064

Hellmer, H.H, Kauker, F., Timmermann, R., & Hattermann, T. (2017). The Fate of the Southern Weddell Sea Continental Shelf in a Warming Climate. *Journal of Climate*, *30*, 4337–4350. https://doi.org/10.1175/JCLI-D-16-0420.1

Holland, D. M., & Jenkins, A. (1999). Modeling Thermodynamic Ice-Ocean Interactions at the Base of an Ice Shelf. *Journal of Physical Oceanography, 29*, 1787–1800, https://doi.org/10.1175/1520-0485(1999)029<1787:MTIOIA>2.0.CO;2

Holland, D. M., Thomas, R. H., de Young, B., Ribergaard, M. H., & Lyberth, B. (2008). Acceleration of Jakobshavn Isbræ triggered by warm subsurface ocean waters. *Nature Geoscience*, *1*(10), 659–664. https://doi.org/10.1038/ngeo316

Howat, I. M., Porter, C., Smith, B. E., Noh, M. J., & Morin, P. (2019). The Reference Elevation Model of Antarctica. *The Cryosphere*, *13*, 665–674. https://doi.org/10.5194/tc-13-665-2019

Ingels, J., Aronson, R. B., Smith, C. R., Baco, A., Bik, H. M., Blake, J. A., et al. (2021). Antarctic ecosystem responses following ice-shelf collapse and iceberg calving: Science review and future research. *Wiley Interdisciplinary Reviews: Climate Change*, *12*(1), 1–28. https://doi.org/10.1002/wcc.682

IPCC (2022). Climate Change 2022: Impacts, Adaptation, and Vulnerability. Contribution of Working Group II to the Sixth Assessment Report of the Intergovernmental Panel on Climate Change [H.-O. Pörtner, D.C. Roberts, M. Tignor, E.S. Poloczanska, K.

Mintenbeck, A. Alegría, M. Craig, S. Langsdorf, S. Löschke, V. Möller, A. Okem, B. Rama (eds.)]. Cambridge University Press. Cambridge University Press, Cambridge, UK and New York, NY, USA, 3056 pp., doi:10.1017/9781009325844.

Jenkins, A., Corr, H. F. J., Nicholls, K. W., Stewart, C. L., & Doake, C. S. M. (2006). Interactions between ice and ocean observed with phase-sensitive radar near an Antarctic ice-shelf grounding line, *Journal of Glaciology, 52*(178), 325–346. https://doi.org/10.3189/172756506781828502

Jenkins, A., Dutrieux, P., Jacobs, S. S., McPhail, S. D., Perrett, J. R., Webb, A. T., & White, D. (2010a). Observations beneath Pine Island Glacier in West Antarctica and implications for its retreat. *Nature Geoscience*, *3*, 468–472. https://doi.org/10.1038/ngeo890

Jenkins, A., Nicholls, K. W., & Corr, H. F. J. (2010b). Observation and parameterization of ablation at the base of Ronne Ice Ahelf, Antarctica. *Journal of Physical Oceanography*, *40*(10), 2298–2312. https://doi.org/10.1175/2010JPO4317.1

Jenkins, A. (2011). Convection-driven melting near the grounding lines of ice shelves and tidewater glaciers. *Journal of Physical Oceanography*, *41*(12), 2279–2294. https://doi.org/10.1175/JPO-D-11-03.1

Jenkins, A. (2021). Shear, Stability, and Mixing within the Ice Shelf–Ocean Boundary Current. *Journal of Physical Oceanography*, *51*(7), 2129–2148. https://doi.org/10.1175/JPO-D-20-0096.1

Joughin, I., Alley, R. B., & Holland, D. M. (2012). Ice-Sheet Response to Oceanic Forcing. *Science*, *338*(November), 1172–1176. https://doi.org/10.1126/science.1226481

Kusahara, K., & Hasumi, H. (2013). Modeling Antarctic ice shelf responses to future climate changes and impacts on the ocean Ž. *Journal of Geophysical Research: Oceans*, *118*(January), 2454–2475. https://doi.org/10.1002/jgrc.20166

Langley, K., Kohler, J., Sinisalo, A., Øyan, M. J., Hamran, S. E., Hattermann, T., et al. (2014a). Low melt rates with seasonal variability at the base of Fimbul Ice Shelf, East Antarctica, revealed by in situ interferometric radar measurements. *Geophysical Research Letters*, *41*(22), 8138–8146. https://doi.org/10.1002/2014GL061782

Langley, K., von Deschwanden, A., Kohler, J., Sinisalo, A., Matsuoka, K., Hattermann, T., et al. (2014b). Complex network of channels beneath an Antarctic ice shelf. *Geophysical Research Letters*, *41*, 1209–1215. https://doi.org/10.1002/2013GL058947

Lauber, J., Hattermann, T., de Steur, L., Darelius, E., Auger, M., Nøst, O. A., & Moholdt, G. (2023a). Warming beneath an East Antarctic ice shelf due to increased subpolar westerlies and reduced sea ice. Nat. Geosci. 16, 877–885. https://doi.org/10.1038/s41561-023-01273-5

Lauber, J., de Steur, L., Hattermann, T., & Nøst, O. A. (2023b). Daily averages of physical oceanography and current meter data from sub-ice-shelf moorings M1, M2 and M3 at Fimbulisen, East Antarctica since 2009 [Data set]. Norwegian Polar Institute. https://doi.org/10.21334/npolar.2023.4a6c36f5

Lindbäck, K., Moholdt, G., Nicholls, K. W., Hattermann, T., Pratap, B., & Thamban, M. (2019). Spatial and temporal variations in basal melting at Nivlisen ice shelf , East Antarctica , derived from phase-sensitive radars. *The Cryosphere*, *13*, 2579–2595. https://doi.org/10.5194/tc-13-2579-2019

Lindbäck, K., Darelius, E., Moholdt, G., Vaňková, I., Hattermann, T., Lauber, J., & de Steur, L. (2023). Basal melt derived from a phase-sensitive radar (ApRES) at Fimbulisen, East Antarctica [Data set]. Norwegian Polar Institute. https://doi.org/10.21334/npolar.2023.1bbf3c47

McConnochie, C. D., & Kerr, R. C. (2018). Dissolution of a sloping solid surface by turbulent compositional convection. *Journal of Fluid Mechanics*, *846*, 563–577. https://doi.org/DOI: 10.1017/jfm.2018.282

Moholdt, G., Padman, L., & Fricker, H. A. (2014). Basal mass budget of Ross and Filchner-Ronne ice shelves, Antarctica, derived from Lagrangian analysis of ICESat altimetry. *Journal of Geophysical Research: Earth Surface*, *119*, 2361–2380. https://doi.org/10.1002/2014JF003171

Morris, A., Moholdt, G., Gray, L., Schuler, T. V., & Eiken, T. (2022). CryoSat-2 interferometric mode calibration and validation: A case study from the Austfonna ice cap, Svalbard.

Remote Sensing of Environment, *269*(February 2021), 112805. https://doi.org/10.1016/j.rse.2021.112805

Mouginot, J., Scheuchl, B., & Rignot., E. (2017). MEaSUREs Antarctic Boundaries for IPY 2007-2009 from Satellite Radar, Version 2. https://doi.org/https://doi.org/10.5067/AXE4121732AD

Nicholls, K. W., Abrahamsen, E. P., Buck, J. J. H., Dodd, P. A., Goldblatt, C., Griffiths, G., et al. (2006). Measurements beneath an Antarctic ice shelf using an autonomous underwater vehicle. *Geophysical Research Letters*, *33*(L08612). https://doi.org/10.1029/2006GL025998

Nicholls, K. W., Abrahamsen, E. P., Heywood, K. J., Stansfield, K., & Østerhus, S. (2008). High-latitude oceanography using the Autosub autonomous underwater vehicle. *Limnology and Oceanography*, *53*(5, part 2), 2309–2320. https://doi.org/10.4319/lo.2008.53.5_part_2.2309

Nicholls, K. W, Corr, H. F. J., Stewart, C. L., Lok, L. B., Brennan, P. V, & Vaughan, D. G. (2015). Instruments and Methods A ground-based radar for measuring vertical strain rates and time-varying basal melt rates in ice sheets and shelves. *Journal of Glaciology*, *61*(230), 1079–1087. https://doi.org/10.3189/2015JoG15J073

Nicholls, K. W. (2018). The study of ice shelf-ocean interaction-techniques and recent results, *29*(3), 222–230. https://doi.org/10.13679/j.advps.2018.3.00222

Nilsson, J., Vallelonga, P., Simonsen, S. B., Sørensen, L. S., Forsberg, R., Dahl-Jensen, D., et al. (2015). Greenland 2012 melt event effects on CryoSat-2 radar altimetry. *Geophysical Research Letters*, *42*(10), 3919–3926. https://doi.org/10.1002/2015GL063296

Padman, L., Fricker, H. A., Coleman, R., Howard, S., & Erofeeva, L. (2002). A new tide model for the Antarctic ice shelves and seas. *Annals of Glaciology*, *34*, 247–254. https://doi.org/10.3189/172756402781817752

Pritchard, H. D., Ligtenberg, S. R. M., Fricker, H. A., Vaughan, D. G., Broeke, M. R. Van Den, & Padman, L. (2012). Antarctic ice-sheet loss driven by basal melting of ice shelves. *Nature*, *484*(7395), 502–505. https://doi.org/10.1038/nature10968

586 Rignot, E., Mouginot, J., & Scheucht, B. (2011). Ice Flow of the Antarctic Ice Sheet. *Science*,
587 *333*, 1427–1431. https://doi.org/10.1126/science.1208336

588 Rignot, E, Jacobs, S., Mouginot, J., & Scheuchl, B. (2013). Ice-Shelf Melting Around
589 Antarctica. *Science*, *341*, 266–270. https://doi.org/DOI: 10.1126/science.1235798

590 Rignot, Eric, Mouginot, J., Scheuchl, B., van den Broeke, M. R., van Wessem, M. J., &
591 Morlighem, M. (2019). Four decades of Antarctic Ice Sheet mass balance from 1979-
592 2017. *Proceedings of the National Academy of Sciences*, *116*(4), 1095–1103.
593 https://doi.org/10.1073/pnas.1812883116

594 Rosevear, M. G., Gayen, B., & Galton-Fenzi, B. K. (2021). The role of double-diffusive
595 convection in basal melting of Antarctic ice shelves. *Proceedings of the National*
596 *Academy of Sciences*, *118*(6), e2007541118. https://doi.org/10.1073/pnas.2007541118

597 Schreiber, T., & Schmitz, A. (2000). Surrogate time series. *Physica D*, *142*, 346–382.
598 https://doi.org/10.1016/S0167-2789(00)00043-9

599 Seroussi, H., Nowicki, S., Payne, A. J., Goelzer, H., Lipscomb, W. H., Abe-Ouchi, A., et al.
600 (2020, September 17). ISMIP6 Antarctica: A multi-model ensemble of the Antarctic ice
601 sheet evolution over the 21st century. *Cryosphere*. Copernicus GmbH.
602 https://doi.org/10.5194/tc-14-3033-2020

603 Stewart, C. L., Christoffersen, P., Nicholls, K. W., Williams, M. J. M., & Dowdeswell, J. A.
604 (2019). Basal melting of Ross Ice Shelf from solar heat absorption in an ice-front
605 polynya. *Nature Geoscience*, *12*, 435–440. https://doi.org/10.1038/s41561-019-0356-0

606 Sun, S., Hattermann, T., Pattyn, F., Nicholls, K. W., Drews, R., & Berger, S. (2019).
607 Topographic Shelf Waves Control Seasonal Melting Near Antarctic Ice Shelf Grounding
608 Lines. *Geophysical Research Letters*, *46*(16), 9824–9832.
609 https://doi.org/10.1029/2019GL083881

610 Thompson, A. F., Stewart, A. L., Spence, P., & Heywood, K. J. (2018). The Antarctic Slope
611 Current in a Changing Climate. *Reviews of Geophysics*, *56*(4), 741–770.
612 https://doi.org/10.1029/2018RG000624

Vaňková, I., Nicholls, K. W., Corr, H. F. J., & Brennan, P. V. (2020). Observations of Tidal Melt and Vertical Strain at the Filchner-Ronne Ice Shelf, Antarctica. *Journal of Geophysical Research: Earth Surface*, *126*. https://doi.org/10.1029/2019JF005280

Vaňková, I., Cook, S., Winberry, J. P., Nicholls, K. W., & Galton-Fenzi, B. K. (2021a). Deriving Melt Rates at a Complex Ice Shelf Base Using In Situ Radar: Application to Totten Ice Shelf. *Geophysical Research Letters*, *48*(7). https://doi.org/10.1029/2021GL092692

Vaňková, I., Nicholls, K. W., & Corr, H. F. J. (2021b). The Nature of Ice Intermittently Accreted at the Base of Ronne Ice Shelf, Antarctica, Assessed Using Phase-Sensitive Radar. *Journal of Geophysical Research: Oceans*, *126*(10). https://doi.org/10.1029/2021JC017290

Vaňková, I., & Nicholls, K. W. (2022). Ocean Variability Beneath the Filchner-Ronne Ice Shelf Inferred From Basal Melt Rate Time Series. *Journal of Geophysical Research: Oceans*, *127*(10). https://doi.org/10.1029/2022JC018879

Vaňková, I., Winberry, J. P., Cook, S., Nicholls, K. W., Greene, C. A., & Galton-Fenzi, B. K. (2023). High spatial melt rate variability near the Totten Glacier grounding zone explained by new bathymetry inversion. *Geophysical Research Letters, 50*, e2023GL102960. https://doi.org/10.1029/2023GL102960

Vreugdenhil, C. A., & Taylor, J. R. (2019). Stratification Effects in the Turbulent Boundary Layer beneath a Melting Ice Shelf: Insights from Resolved Large-Eddy Simulations. *Journal of Physical Oceanography*, *49*(7), 1905–1925. https://doi.org/https://doi.org/10.1175/JPO-D-18-0252.1